Journal of Molecular Structure 1266 (2022) 133474

Contents lists available at ScienceDirect

Journal of Molecular Structure

journal homepage: www.elsevier.com/locate/molstr

Structural characterization and computational investigations of three fluorine-containing ligands with a terphenyl core

Ioan-Andrei Dascalu[a,*], Dragos-Lucian Isac[a], Sergiu Shova[a], Mihaela Balan-Porcarasu[a], Narcisa-Laura Marangoci[a], Mariana Pinteala[a], Christoph Janiak[b]

[a] Petru Poni Institute of Macromolecular Chemistry, 41A Aleea Gr. Ghica Vodă, Iaşi 700487, Romania
[b] Institute for Inorganic and Structural Chemistry, Heinrich-Heine University Düsseldorf, Düsseldorf 40225, Germany

ARTICLE INFO

Article history:
Received 20 April 2022
Revised 24 May 2022
Accepted 6 June 2022
Available online 7 June 2022

Keywords:
Terphenyl dicarboxylic acids
Ditopic ligands
Single crystal X-ray diffraction
Hirshfeld surface
Molecular modeling

ABSTRACT

Three linear terphenyl dicarboxylic acids with various number of fluorine addends have been prepared in a direct manner through Suzuki–Miyaura coupling. The central phenyl ring of the compounds is substituted with two or four fluorine atoms or two trifluoromethyl groups respectively. The structure and geometry of the dicarboxylic acids were confirmed by single crystal X-ray diffraction. The molecular structure of the three fluorine containing ligands was studied through molecular modeling methods. Hirshfeld surface analysis for each compound is presented.

1. Introduction

The chemistry of metal-organic frameworks is a rapidly growing research field owing to the practical potential of this class of porous compounds [1–3]. Metal-organic frameworks are extended two- or three-dimensional networks comprised of metal nodes and rigid organic ligands joined together by coordination bonds [4]. The introduction of the reticular synthesis concept [5], that was described as the adequate design or selection of existing ligands and inorganic building blocks and their subsequent strong bonding into a predetermined ordered network, afforded a new perspective in the development of these materials. In this respect, the size, shape and type of coordinating groups are the main factors to be taken into account in the design of ligands for metal-organic frameworks [6]. The aforementioned characteristics are responsible for the type of network and its stability, whereas the capacity to interact with guest molecules is mainly ensured by certain atoms or chemical groups present in the ligand molecule. The inclusion of these elements that facilitate the host-guest interactions in the final structure of a given metal-organic framework is secured either through rigorous ligand design, or by means of post-synthetic modifications [7,8]. The post-synthesis modification strategy is limited by the chemical and thermal stability of the network, the size of the network pores, or type and size of the used reagents [9].

The use of partially fluorinated or per-fluorinated ligands in the synthesis of metal-organic frameworks has led so far to interesting results [10–15]. The appealing feature in the development and use of this type of ligand is the small size of the fluorine atom, which does not significantly reduce the free volume within a porous coordination polymer. Moreover, the polarized C–F bond enables potential interactions with the guest molecules within the framework. In addition, the hydrophobicity of the pore surface that is induced by the presence of the fluorine atoms has been shown to substantially improve the hydrolytic resistance of the network, and to assist the accommodation of hydrophobic guests by blocking the absorption of water almost completely while allowing the uptake of hydrophobic molecules [16]. Also, it has been previously reported that an increase of the number of fluorine atoms in the pores of a metal-organic framework leads to a preferential uptake of hydrogen and carbon dioxide [17,18]. Taking into account the significance of fluorine-containing ligands for the development of novel coordination polymers with potential applications, the present report aims at describing one step synthetic approaches towards three fluorinated terphenyl-dicarboxylic acids that can be subsequently used in the preparation of metal-organic frameworks. Computational studies of these fluorine-substituted acids have highlighted the influence that the presence of this halogen has towards the reactivity and conformational effects of the ligands.

* Corresponding author.
E-mail address: idascalu@icmpp.ro (I.-A. Dascalu).

https://doi.org/10.1016/j.molstruc.2022.133474
0022-2860/

2. Experimental

2.1. Materials, methods and instruments

All chemicals were purchased from commercial suppliers (Sigma–Aldrich, TCI Europe N.V., Merck KGaA) and used as received. 1,4-Dibromo-2,5-bis(trifluoromethyl)benzene required as starting material in the synthesis of compound **3** was prepared through bromination of 1,4-bis(trifluoromethyl)benzene as described previously [19]. Fourier Transform-Infrared (FT-IR) spectra were recorded on a FT-IR Bruker Vertex 70 spectrophotometer in transmission mode using KBr pellets. The intensity of the absorption bands is given as very strong (vs), strong (s), medium (m), weak (w) and very weak (vw). All spectra were collected at a 2 cm^{-1} resolution, in the mid-IR range (4000–400 cm^{-1}). CHN elemental analysis was performed on a Vario-EL-III elemental analyzer. The melting point of the compounds measured on a MEL-TEMP capillary melting point apparatus from ambient temperature up to 400 °C. NMR spectra were recorded on a Bruker Avance NEO spectrometer operating at 400 MHz, with a 5 mm probe for direct detection of H, C, F, Si. DMSO–d_6 was used as solvent and the spectra were calibrated on the residual peak of the solvent (δ= 2.51 for ^{1}H and δ= 39.47 for ^{13}C). The spectra were recorded at room temperature using the standard parameter sets provided by Bruker. The ^{13}C NMR spectra for **2** and **1** were recorded with 25k scans and 14k of scans, respectively. The signal assignments in the proton and carbon spectra were done using proton–carbon correlation experiments: H,C-HSQC and H,C-HMBC. The numbering of the atoms in the structure of the compounds (Fig. 1) corresponds to that from the X-ray structures (Fig. 2).

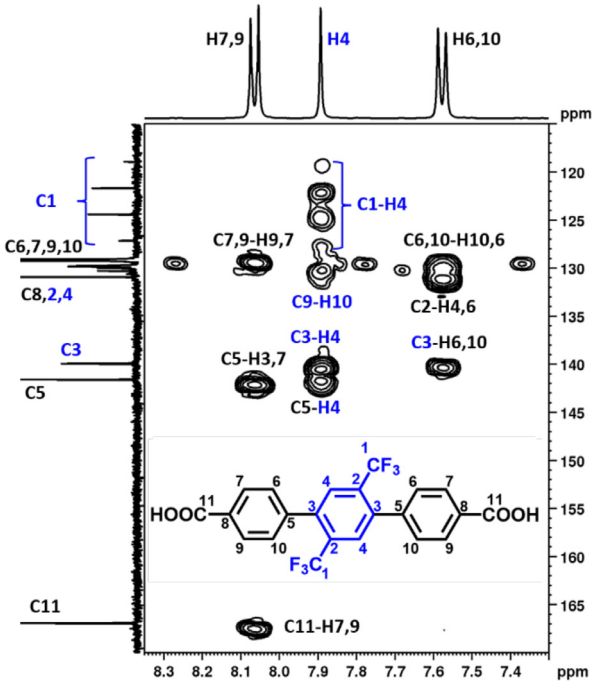

Fig. 1. H,C-HMBC spectrum (DMSO–*d6*, 400 MHz) for **3** and assignment of the signals.

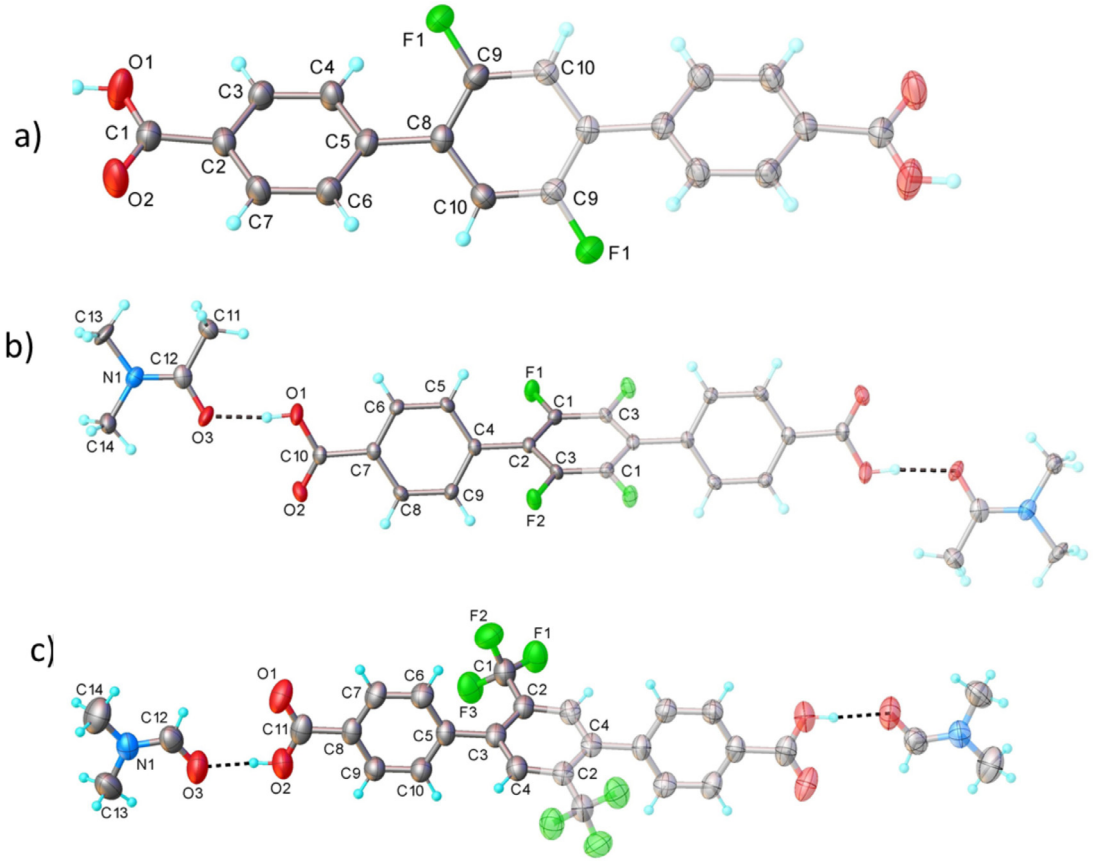

Fig. 2. X-ray molecular structure with atom labeling and thermal ellipsoids at 50% probability for **1** (a), **2** (b) and **3** (c). Symmetry generated fragments are shown with faded colours. Only the major position occupied by disordered fluorine atoms in the molecule of compound **1** is shown.

Table 1
Crystal data and details of data collection.

	1	**2**	**3**
Empirical formula	$C_{20}H_{12}F_2O_4$	$C_{28}H_{28}F_4N_2O_6$	$C_{28}H_{26}F_6N_2O_6$
Fw	354.30	564.52	600.51
Space group	*P*-1	*C*2/*c*	*C*2/*c*
a [Å]	3.7783(4)	32.7766(15)	30.924(2)
b [Å]	7.9284(8)	5.7324(3)	8.1884(6)
c [Å]	13.1369(12)	13.9691(6)	11.1489(10)
α [°]	74.849(8)	90	90
β [°]	82.243(8)	101.354(4)	92.406(8)
γ [°]	82.813(9)	90	90
V [Å^3]	374.71(7)	2573.3(2)	2820.6(4)
Z	1	4	4
ρ_{calcd} [g cm^{-3}]	1.570	1.457	1.414
Crystal size [mm]	0.20 × 0.10 × 0.05	0.20× 0.15 × 0.04	0.20 × 0.10 × 0.05
T [K]	293	160	180
μ [mm^{-1}]	0.126	0.121	0.125
2Θ range [°]	5.3 to 50.0	5.0 to 50.0	5.1 to 50.0
Reflections collected	2756	24212	7106
Independent reflections	1331[R_{int}=0.0213]	15318[R_{int}=0.0428]	2496[R_{int}=0.0374]
Data/restraints/parameters	1331/0/123	3401/0/186	2496/1/202
R_1 [a]	0.0459	0.0436	0.0557
wR_2 [b]	0.1022	0.1067	0.1166
GOF[c]	1.032	1.001	1.028
Largest diff. peak/hole [e Å^{-3}]	0.19/−0.18	0.30/−0.21	0.13/−0.15
CCDC	2,164,600	2,164,601	2,164,602

[a] $R_1 = \Sigma||F_o| - |F_c||/\Sigma|F_o|$. [b] $wR_2 = \{\Sigma[w(F_o^2 - F_c^2)^2]/\Sigma[w(F_o^2)^2]\}^{1/2}$. [c] GOF = $\{\Sigma[w(F_o^2 - F_c^2)^2]/(n - p)\}^{1/2}$, where *n* is the number of reflections and *p* is the total number of parameters refined.

Single crystal X-ray diffraction measurements were carried out with a Rigaku Oxford-Diffraction XCALIBUR E CCD diffractometer equipped with graphite-monochromated MoKα radiation. Single crystals were positioned at 40 mm from the detector and 280, 386 and 419 frames were measured each for 30 s, 30 s and 50 s over 1° scan width for **3, 1** and **2**, respectively. The unit cell determination and data integration were carried out using the CrysAlis package of Oxford Diffraction [20]. The structures were solved by Intrinsic Phasing using Olex2 [21] software with the SHELXT [22] structure solution program, and refined by full-matrix least-squares on F^2 with SHELXL-2015 [23] using an anisotropic model for non-hydrogen atoms. The structure **2** was determined from the non-merohedral twin. The twin law corresponds to the rotation of 180° around direction [0.91 0.0 0.42] in direct space. The refinement showed that the fractional contributions of the two domains are of 0.53/0.47. The hydrogen atoms attached to carbon were placed geometrically and constrained to ride with d_{CH} = 0.96 Å and U_{iso}values of 1.2 Ueq of the parent atoms. The hydrogen atoms involved in hydrogen bonding were localized from difference Fourier maps and their positional parameters were verified according to hydrogen bonds geometry. The positional parameters of disordered atoms in the crystal of **3** and **1** were refined with necessary imposed restraints on geometry and displacement parameters available in SHELXL program. The molecular plots were obtained using the Olex2 program. The crystallographic data and refinement details are presented in Table 1, while bond lengths and angles are summarized in Tables S1, S3 and S5.

Theoretical calculations were carried out using the density functional theory (DFT) with Gaussian G 16 program [24]. APFD functional and 6–31+*G* (d,p) Popple basis set were selected as theory level [25,26]. The selected APFD density functional provides good results relating to the conformational as well as the electronic effects for both organic [27] and inorganic compounds [28], being in agreement with the experimental data. The computational results were analyzed and depicted with Gauss View 6 and Avogadro software [29,30].

The first stage of theoretical investigation, which involved an optimization procedure for the target compounds (**1, 2**, and **3**), was performed using the APFD/6–31+*G*(d,p) method. The equilibrium molecular geometry was confirmed by Hessian calculation, and no imaginary frequency was obtained. In the geometry optimization, an ultrafine integration (int=ultrafine keyword in Gaussian) grid and tight convergence thresholds (opt=tight, scf=tight keywords in Gaussian) were used.

The Highest Occupied Molecular Orbital-Lowest Unoccupied Molecular Orbital (HOMO-LUMO) representations, the energy gap, and the electrostatic surface potential (ESP) were represented for the optimized structures. The non-covalent interplays were estimated with Multiwfn [31] and NCIPLOT program [32,33]. Likewise, for representation of weak interactions the VMD 1.9.3 [34] and Gnuplot software's [35] have been used.

2.2. Synthesis

2.2.1. Synthesis of *2′,5′-difluoro-[1,1′:4′,1′′-*terphenyl*]–4,4′′-dicarboxylic acid 1*

To a solution of 1,4-dibromo-2,5-difluorobenzene (1.09 g, 4 mmol) and 4-carboxyphenylboronic acid (1.67 g, 10 mmol) in tetrahydrofuran (THF, 150 mL), a solution of potassium carbonate (5.95 g, 43.05 mmol) in water (30 mL) was added. The resulting mixture was then subjected to repeated cycles consisting of argon sparging followed by degassing under vacuum before tetrakis(triphenylphosphine)palladium(0) (0.138 g, 0.12 mmol) was added. The reaction mixture was refluxed under an inert argon atmosphere while being vigorously stirred for 72 h. Then, the pH of the cooled dark gray dispersion was brought to 1–2 by gradual addition of aq. 3 M HCl under efficient stirring. The resulting precipitate was collected by filtration, washed thoroughly with water, then ethanol, and air-dried. The solid was suspended in the minimum amount of boiling *N,N*-dimethylformamide (DMF, 50 mL), and then the insoluble material was removed by hot filtration. Upon cooling, the diacid separated out as off-white needles (1.13 g, 79%), m.p. > 400 °C; FT-IR (ν, cm^{-1}: 2669 (vw), 2545 (vw), 1934 (vw), 1689 (vs), 1608 (s), 1569 (w), 1523 (m), 1485 (s), 1427 (s), 1390 (s), 1321 (s), 1292 (s), 1166 (m), 1110 (m), 1037 (vw), 1010 (w), 923 (m), 893 (m), 854 (s), 815 (w), 767 (s), 702 (s), 667 (w), 549 (s), 505 (m), 466 (m); Anal. Calculated for $C_{20}H_{12}F_2O_4$: C, 67.81; H, 3.41. Found: C, 68.13; H, 3.53. ^{1}H NMR (400.13 MHz, δ,

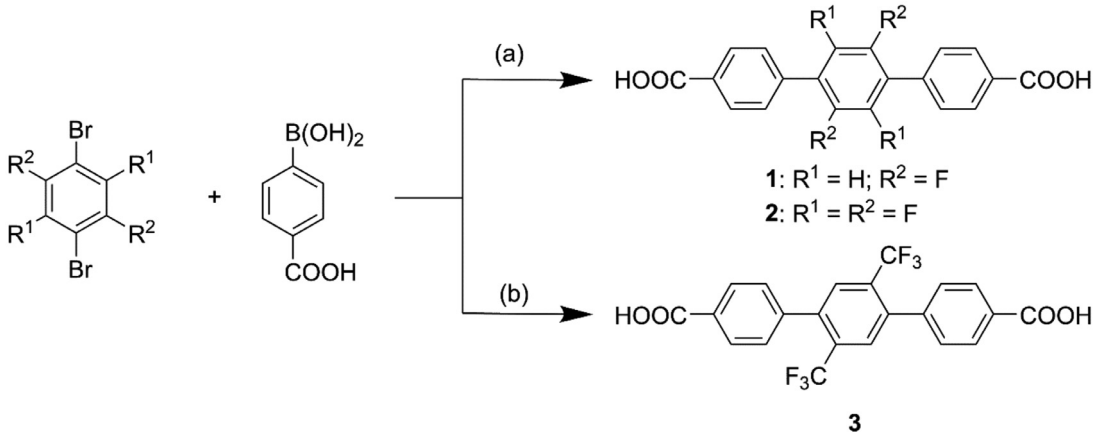

Scheme 1. Synthetic approach towards the three reported ligands. Reaction conditions: (a) $Pd(PPh_3)_4$, K_2CO_3, THF:water (5:1 v/v), reflux, 72 h; (b) $Pd(PPh_3)_4$, K_2CO_3, dioxane:ethanol:water (4:1:1 v/v/v), reflux, 72 h.

ppm): 13.18 (s, 2H, H-1), 8.08 (d, J = 8.3 Hz, 4H, H-3, H-7), 7.79 (d, J = 8.2 Hz, 4H, H-4, H-6), 7.69 (t, J = 8.8 Hz, 2H, H-10). ^{13}C NMR: (100.6 MHz, δ, ppm): 167.0 (C-1), 156.1–154.1 (d, J = 242.3 Hz, CF-9), 137.7 (C-5), 130.8 (C-2), 129.7 (C-3, C-7), 129.1 (C-4, C-6), 128.4 (t, J = 12 Hz, C-8), 117.9 (dd, J = 30 Hz, J = 7 Hz, CH-9, CH-10) ^{19}F NMR (376.4 MHz, δ, ppm): −122.5 (t, J = 8.8 Hz, F-1).

*2.2.2. Synthesis of 2′,3′,5′,6′-tetrafluoro-[1,1′:4′,1″-*terphenyl*]–4,4″-dicarboxylic acid 2*

Starting from 1,4-dibromo-2,3,5,6-tetrafluorobenzene (1.24 g, 4 mmol) instead of 1,4-dibromo-2,5-difluorobenzene, a synthetic procedure that was identical to that previously described in detail for the preparation of **1** and afforded a crude material that was suspended in the minimum volume of boiling DMF (45 mL). Removal of insoluble impurities by hot filtration and subsequent slow cooling to room temperature gave colorless crystals (1.2 g, 76%), m.p. > 400 °C; FT-IR (ν, cm^{-1}): 2673 (w), 2547 (w), 1695 (vs), 1610 (m), 1566 (w), 1477 (s), 1423 (s), 1402 (s), 1296 (s), 1188 (w), 1114 (w), 1018 (w), 981 (s), 910 (m), 856 (m), 837 (w), 788 (m), 767 (m), 748 (vw), 700 (m), 547 (m), 487 (w); Anal. Calculated for $C_{28}H_{28}F_4N_2O_6$: C, 59.58; H, 4.99, N, 4.96. Found: C, 59.99; H, 4.43, N, 5.11. ^{1}H NMR (400.13 MHz, δ, ppm): 13.25 (s, 2H, H-10), 8.14 (d, J = 8.4 Hz, 4H, H-6, H-8), 7.74 (d, J = 8.1 Hz, 4H, H5, H-9). ^{13}C NMR: (100.6 MHz, δ, ppm): 167.0 (C-10), 156.1–154.1 (d, J = 251.5 Hz, C-1, C-3), 131.8 (C-7), 130.8 (C-4), 130.3 (C-5, C-9), 129.6 (C-6, C-8), 128.4 (m, C-2). ^{19}F NMR (376.4 MHz, δ, ppm): −143.7 (F-1, F-2).

*2.2.3. Synthesis of 2′,5′-bis(trifluoromethyl)-[1,1′:4′,1″-*terphenyl*]–4,4″-dicarboxylic acid 3*

1,4-Dibromo-2,5-bis(trifluoromethyl)benzene (1.49 g, 4 mmol) and 4-carboxyphenylboronic acid (1.67 g, 10 mmol) were dissolved under efficient stirring in a mixture of dioxane and 96% ethanol (150 mL, 4:1 *v*/*v*, respectively). The organic solution was combined with a solution of potassium carbonate (5.8 g, 42 mmol) in water (30 mL), and the resulting mixture was then thoroughly sparged with argon before tetrakis(triphenylphosphine)palladium(0) (0.138 g, 0.12 mmol) was added. The reaction mixture was next refluxed under argon with vigorous stirring for 72 h. After cooling to room temperature, the reaction mixture was filtered and then treated with aq. 3 M HCl under efficient stirring until pH reached 1–2. The resulting precipitate was filtered, washed thoroughly with water, and air-dried. Recrystallization from DMF (5 mL), accompanied by hot filtration of the suspension yielded upon cooling white needles (1.48 g, 81%), m.p. > 400 °C; FT-IR (ν, cm^{-1}): 2671 (vw), 2544 (vw), 1697 (vs), 1608 (m), 1566 (w), 1523 (w), 1498 (w), 1417 (s), 1286 (s), 1247 (s), 1136 (vs), 1087 (s), 1029 (m), 929 (w), 904 (m), 858 (m), 808 (w), 777 (m), 757 (w), 705 (s), 659 (w), 621 (w), 588 (w), 551 (s), 536 (m), 482 (w); Anal. Calculated for $C_{28}H_{26}F_6N_2O_6$: C, 56.01; H, 4.36, N, 4.66. Found: C, 56.41; H, 4.22, N, 4.81. ^{1}H NMR (400.13 MHz, δ, ppm): 13.17 (s, 2H, H-11), 8.06 (d, J = 8.3 Hz, 4H, H-7, H-9), 7.89 (s, 2H, H-4), 7.58 (d, J = 8.2 Hz, 4H, H-6, H-10). ^{13}C NMR: (100.6 MHz, δ, ppm): 166.9 (C-11), 141.6 (C-5), 139.9 (C-3), 130.9 (C-7), 130.1 (q, J = 31 Hz, C-2), 129.8 (d, J = 5 Hz, C-4), 129.2 (C-6, C-10), 129.0 (C-7, C-9), 123.0 (q, J = 274.9 Hz, C-1). ^{19}F-NMR (376.4 MHz, δ, ppm): −56.1 (F-1, F-2, F-3).

3. Results and discussion

3.1. Chemistry

Assembly of polyaromatic structures through the Suzuki–Miyaura cross-coupling reaction [36] employing bromine- or iodine-substituted aromatics as substrates and substituted phenylboronic acid as organoborane partner is a common synthetic strategy for the preparation of structurally diverse aromatic compounds useful as organic ligands [37]. Owing to their improved solubility in organic solvents that allows facile post-synthetic work-up, commercially available, albeit more expensive, alkoxycarbonylarylboronic acids have been used as alternative reagents to the corresponding carboxyaryl boronic acids in the cross-coupling reaction. In fact, two of the ligands reported in this study, namely **2** and **3**, have been recently prepared through a two-step procedure that involves firstly the Suzuki–Miyaura reaction of 4-methoxycarbonylphenylboronic acid with the appropriately substituted haloaromatic, followed by a base-catalyzed hydrolysis stage [38]. The advantage of this two-step approach is that it allows easy access to high-purity diesters of the desired ligand through recrystallization of these intermediates from common organic solvents with low boiling points prior to their transformation into the sparingly soluble diacids. One of the goals of the current work is to investigate the feasibility of a one-step synthetic approach towards fluorine-containing organic ligands, as presented in Scheme 1.

The coupling proceeds smoothly under the particular reaction conditions identified in this study for each of the three target compounds, affording pure substances with good yields (up to 80%) after recrystallization. Although some slight loss in the desired compounds incurred during removal of spent palladium and purification stage, the yields are still superior to those recorded for the two-step synthetic approach of **2** and **3** [38]. It has been

noticed in the course of this work that the presence of fluorine as a substituent directly attached to the aromatic terphenyl core renders compounds **1** and **2** practically insoluble in common organic solvents (such as lower alcohols, acetone, chloroform, dichloromethane, tetrahydrofuran, etc.). A 5:1 THF:water mixture has been found to be efficient as reaction medium in the preparation of **1** and **2**, as it dissolves adequately both reactants in the cross-coupling reaction, while the resulting potassium salt of the aforementioned compounds gradually precipitates and forms a thick suspension at the end of the reaction time. However, initial attempts to use the same reaction medium in the synthesis of **3** was accompanied by very low yields of the target compound, presumably owing to poorer reactivity of 1,4-dibromo-2,5-bis(trifluoromethyl)benzene in the cross-coupling reaction compared to 1,4-dibromo-2,5-difluorobenzene and 1,4-dibromo-2,3,5,6-tetrafluorobenzene. Nonetheless, replacement of THF with a mixture of dioxane and ethanol was shown to significantly improve the reactivity of the trifluoromethyl-substituted substrate, and to allow the reaction to occur with increased conversion of this substrate into the target compound **3**. In this case, the solubility of the potassium salt of **3** in the solvent mixture facilitated the easy removal of most of the spent palladium catalyst through filtration at the end of the reaction time and prior to the acid treatment required for the isolation of the dicarboxylic acid **3**.

All three compounds were purified through recrystallization of the crude products from DMF. Hot filtration of insoluble impurities consisting of spent palladium was required in particular in the purification of compound **1** and **2**. Hot filtration was also deemed desirable in the purification of crude **3**, although the content of mechanical impurities in this material was substantially lower than in the case of the materials isolated after the work-up of the other two target compounds. Use of DMF as recrystallization solvent also produced single crystals suitable for X-ray investigations in the case of **1** and **3**, but not **2**. However, an attempt to recrystallize the latter compound from *N,N*-dimethylacetamide (DMAc) afforded also single crystals of this diacid that were found to be appropriate for X-ray studies.

3.2. Structural characterization of the target compounds

3.2.1. FT-IR spectroscopy

The FT-IR spectra of the target compounds (Figs. S1–S3) are very similar, apart for a few minor differences that will be detailed below. The presence of the carboxyl groups in the structure of these compounds is associated with the most intense absorption band in the spectra (1689 cm^{-1} for **1**, 1695 cm^{-1} for **2** and 1697 cm^{-1} for **3**), which has been assigned to the stretching vibration of the carbonyl group. In the case of **1**, the very weak band at 3431 cm^{-1} was assigned to the hydroxyl group stretching vibration, while the corresponding band is less intense for **2**, and it is completely absent for **3**. The stretching vibration of the bond between an aromatic carbon and fluorine can be easily identified as the strong absorption band centered at 1292 cm^{-1} for **1** and at 1296 cm^{-1} for **2** [39]. In the particular case of **3**, the out-of-phase stretching vibrations in the trifluoromethyl group have been associated with the relatively broad band centered at 1136 cm^{-1} and with an adjacent less intense band at 1087 cm^{-1}[39].

3.2.2. NMR spectroscopy

NMR spectra of the compounds reported in this study correspond to the proposed structures. Because of their structural high symmetry and high degree of substitution of the molecules, the ^{1}H NMR and ^{19}F NMR spectra show few signals (Figs. S4–S9). ^{1}H NMR spectrum of each of these compounds shows a broad peak for the carboxylic protons at 13.17 ppm (**3**), 13.25 ppm (**2**) and 13.18 ppm (**1**). The protons for the terminal *p*-disubstituted benzene rings give two doublets at 8.06 and 7.58 ppm for **3**, 8.08 and 7.79 ppm for **1** and 8.14 and 7.74 ppm for **2**. The protons from the central fluorine-substituted phenyl ring of **3** resonate at 7.89 ppm, while the ones in **1** give a triplet at 7.69 ppm. The fluorine atoms in each compound are magnetically equivalent and give peaks in the ^{19}F NMR spectra at characteristic chemical shift values, namely at −56.1 ppm for fluorine atoms in trifluoromethyl groups of **3**, and at −143.7 ppm and −122.5 ppm for the fluorine atoms directly attached to the aromatic rings in **2** and **1**, respectively. In the ^{13}C NMR spectra of each compound (Figs. S10–S12), the carbon atom in the carboxylic group has been assigned a peak at about 167 ppm, while the aromatic carbon atoms in the terminal phenyl rings appear as four distinct peaks. The signals for the carbons in the central fluorine-substituted phenyls have a more complex pattern which consists of multiplets, owing to ^{13}C – ^{19}F couplings over one, two or three bonds. Thus, in the ^{13}C NMR spectrum of **3,** two quartets, one for the carbon atoms of the trifluoromethyl group (123 ppm) and one for the phenyl quaternary carbons substituted with the trifluoromethyl group (130.1 ppm), can be observed. The later quartet partially overlaps the doublet associated with the carbon atom *ortho* to trifluoromethyl. The carbon atoms substituted with fluorine in the structure of **1** give a doublet at 155.1 ppm, their neighboring tertiary carbon atoms give a triplet at 128.4 ppm, while their neighboring quaternary carbon atoms give a doublet of doublets at 117.9 ppm. The ^{13}C NMR spectrum of **2** shows two sets of complex multiplets for the carbon atoms in the fluorine-substituted phenyl ring, one centered at 143.4 ppm for the -CF carbons, and the other centered at 118.9 ppm corresponding to the quaternary carbons bound to the terminal phenyl rings. The exact assignment of the peaks from the ^{1}H and ^{13}C NMR spectra was carried out using 2D H,C–HSQC and H,C–HMBC experiments (Figs. S13–S17). The H,C–HMBC experiments showed correlations between the protons and the carbons in the terminal phenyl rings and the ones in the central phenyl ring (as seen in Fig. 1). Thus, long range correlations between C8 in the central fluorine-substituted phenyl ring and H4 and H6 in the carboxyl-substituted phenyl rings can be noticed for all three compounds. An additional correlation between C5 and H9 is also evident in the 2D NMR spectra of **3** and **1**.

3.3.3. Single crystal structure

The X-ray molecular structures of the three compounds reported in this work, as they resulted from the X-ray diffraction study, are shown in Fig. 2. There are no co-crystallized solvate molecules in the crystal of **1**, while one molecule of **2** crystallizes with two dimethylacetamide molecules, and each molecule of **3** crystallizes with two dimethylformamide molecules. As shown in Fig. 2, the solvent molecules act as acceptors in hydrogen bonding with carboxylate groups, which serve as donors of protons in both crystals. The molecules of **1, 2** and **3** exhibit intrinsic crystallographic imposed symmetry, with the inversion center located in middle of the central phenyl ring. It is noteworthy that fluorine atoms are disordered between two positions (atoms C9 and C10) with occupancy factors of 0.78 and 0.22. Likewise, the carboxylate proton is disordered between two oxygen atoms with equal probability. Because of the steric hindrance induced by the substituents in the central aromatic rings, the three molecules exhibit a non-planar configuration. The dihedral angle between the central and peripheral rings is of 136.6(1)°, 122.4(1)° and 117.1(1)° for **1, 2** and **3**, respectively. The crystal packing for all three compounds also shows close similarities. Thus, the components of the structure interact through a extended system of O-H···O and C-H···O hydrogen bonding. The geometry of the hydrogen bonds is summarized in Tables S2, S4 and S6. In the crystal of **1**, these interactions are complemented by π-π stacking interactions, which determine the

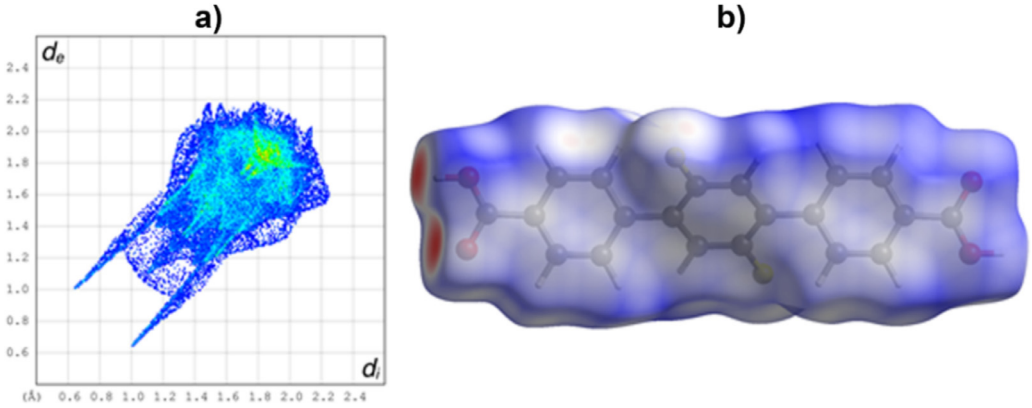

Fig. 3. (a) 2D fingerprint plot for the compound **1** entity in **1** with the sharp features pointing to the lower left corner being due to O-H···O interactions (d_i and d_e are the distances from the surface to the nearest atom interior and exterior to the surface, respectively). Breakdown of the plot to contributions from O···H, F···H, H···H, C···H, F···F, C···C, F···C and O···C close intermolecular contacts is shown in Fig. S21; (b) Hirshfeld surface mapped with the d_{norm} property. The red spots represent the closest contacts and blue the most distant contacts. Breakdown of the d_{norm} property is shown in Fig. S21.

formation of two dimensional supramolecular layers, as shown in Fig. S18a. The crystal structure is further built up through parallel packing of discrete, weakly interacting 2D architectures (Fig. S18b).

No stacking interactions were observed in the crystal structure of **2** and **3**, which means that the crystal packing is essentially determined by intermolecular hydrogen bonding involving solvate *N,N*-dimethylacetamide molecules for **2** and *N,N*-dimethylformamide molecules for **3**. In the crystal of **2**, the solvate molecules act as bridges, being involved in O–H···O H-bonding as acceptors and C-H···O H-bonds as donors of protons. As a result, the **2** molecules are packed to form a supramolecular three-dimensional network, which is illustrated in Fig. S19. On the other hand, dimethylformamide molecules in the crystal of **3** act only as acceptor in O-H···O in hydrogen bonds with carboxylate groups. In this case, the association of **3** molecules occurs through direct C-H···O, and the resulting main crystal structure motif is a one-dimensional architecture, as shown in Fig. S20.

3.3. Theoretical investigation of the target compounds

3.3.1. Hirshfeld surface analysis

Hirshfeld surface analysis of 1. The supramolecular packing evidenced in the solid crystalline form of **1** through X-ray analysis can also be investigated by means of intermolecular interactions with Hirshfeld surfaces using the program CrystalExplorer [40], as previously outlined in literature [41]. A molecule of compound **1** having all disorder removed was used as molecular unit in this investigation. Thus, the minor contributions to the supramolecular packing of fluorine and hydrogen atoms in the central ring were omitted. In addition, only H1 from one carboxyl group was maintained, while H2 was removed. All remaining atoms were given full occupancy. Fig. 3 shows the 2D fingerprint plot for **1**, and this representation encodes the supramolecular interactions (such as the O-H···O interactions) in the characteristic two sharp features pointing to the left bottom part of the plot. The Hirshfeld surface for **1**, which provides an overlay of all contributions from close intermolecular contacts, is given in Fig. 3, and displays these O-H···O intermolecular contacts through the red circles on the d_{norm} surface. The relative contributions to the Hirshfeld surface area in **1** due to intermolecular contacts are as follows: H···O (including C-H···O) 25.8%, H···F 13.9%, H···H 26.5% H···C (e.g. C–H···π) 11.5%, FC···C (e.g. $\pi\cdots\pi$) 14.0%, F···C 3.9% and O···C 3.3% (see Table S7 for the comparative listing of these contributions).

Hirshfeld surface analysis of 2. The DMF-**2**-DMF entity was used for the molecular unit. Hence, the O-H···O interactions from **2** to the DMF molecules are not part of this analysis. The 2D fingerprint plot for **2** in Fig. 4a encodes the supramolecular interactions, but different to **1** and **3** shows now characteristic sharp features (Figs. 3 and 5). The Hirshfeld surface for **2** in Fig. 4b displays some weak C-H···O intermolecular contacts by the red circles on the d_{norm} surface. The Hirshfeld surface represents an overlay of all contributions from close intermolecular contacts. The relative contributions to the Hirshfeld surface area in **2** due to intermolecular contacts are H···O (including C-H···O) 20.3%, H···F 14.8%, H···H 36.8% H···C (e.g. C–H···π) 13.4%, F···F 1.9%, C···C (e.g. $\pi\cdots\pi$) 3.6%, and F···C 5.8% (see Table S7 for the comparative listing of these contributions).

Hirshfeld surface analysis of 3. The DMF-**3**-DMF entity was used as the molecular unit in the calculation of the Hirshfeld surface for this compound. Hence, the O–H···O interactions between **3** and the DMF molecules (Fig. 2c) are not part of this analysis. The 2D fingerprint plot for **3** that is shown in Fig. 5a illustrates the supramolecular interactions in this entity, such as the C-H···O interactions, as the two characteristic sharp features pointing to the left bottom part of the plot. The Hirshfeld surface representation for **3**, given in Fig. 5b, evidences these C–H···O intermolecular contacts through the red circles on the d_{norm} surface. The relative contributions to the Hirshfeld surface area in **3** due to intermolecular contacts are as follows: H···O (including C–H···O) 17.1%, H···F 23.8%, H···H 33.5% H···C (e.g. C–H···π) 10.6%, F···F 3.8%, C···C (e.g. $\pi\cdots\pi$) 4.0%, and F···C 3.5% (see Table S7 for the comparative listing of these contributions).

3.3.2. Molecular modeling

Optimization of the molecular geometry for each compound was performed with APFD/6–31+*G*(d,p) method. The computational results are represented in Figs. 6–8. The molecular parameters (bond lengths and dihedral angles) computed at APFD/6–31+*G*(d,p) level of theory were compared with the experimental data provided by the X-ray study. For clear visualization, some bond lengths and dihedral angles from the X-ray representation were highlighted in yellow (Figs. 6–8). In addition, the labels of the atoms in the case of optimized molecular systems were indicated.

The theoretical results show that the presence of the substituents (either fluorine atoms or trifluoromethyl groups) in the central phenyl ring in *ortho* positions relative to the terminal phenyl rings induces a twisting effect in all target compounds. This twisting effect could be observed from the value of the dihedral angles C15-C14-C10-C11 and C8-C7-C2-C3 that are formed between the plane of each of the terminal phenyl rings and the central substituted phenyl (Figs. 6–8). The values of the aforementioned dihe-

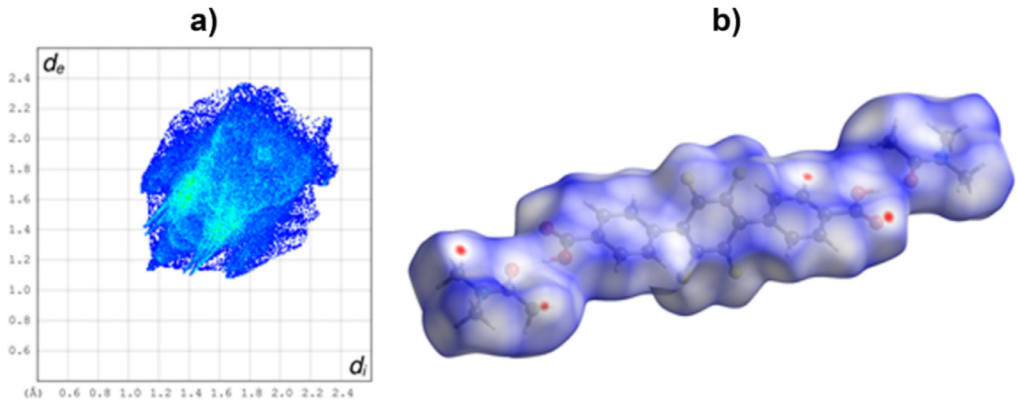

Fig. 4. (a) 2D fingerprint plot for the DMAc-**2**-DMAc entity in **2** (d_i and d_e are the distances from the surface to the nearest atom interior and exterior to the surface, respectively). Breakdown of the plot into the contributions from O···H, F···H, H···H, C···H, F···F, C···C and F···C close intermolecular contacts is shown Fig. S22. (b) Hirshfeld surface mapped with the d_{norm} property. The red spots represent the closest contacts and blue the most distant contacts. Breakdown of the d_{norm} property is shown Fig. S22.

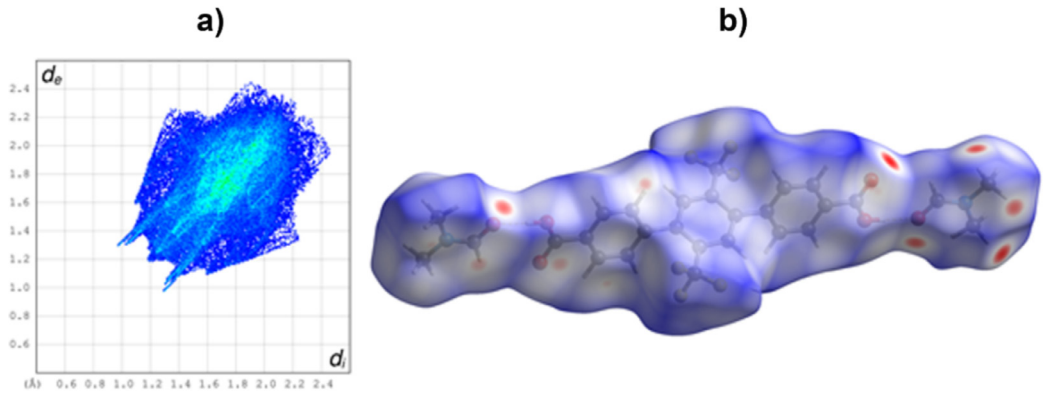

Fig. 5. (a) 2D fingerprint plot for the DMF-**3**-DMF entity in **3** with the short but still sharp features pointing to the lower left corner being due to C-H···O interactions (d_i and d_e are the distances from the surface to the nearest atom interior and exterior to the surface, respectively). Breakdown of the plot into the contributions from O···H, F···H, H···H, C···H, F···F, C···C and F···C close intermolecular contacts is shown in Fig. S23; (b) Hirshfeld surface mapped with the d_{norm} property. The red spots represent the closest contacts and blue the most distant contacts. Breakdown of the d_{norm} property is shown in Fig. S23.

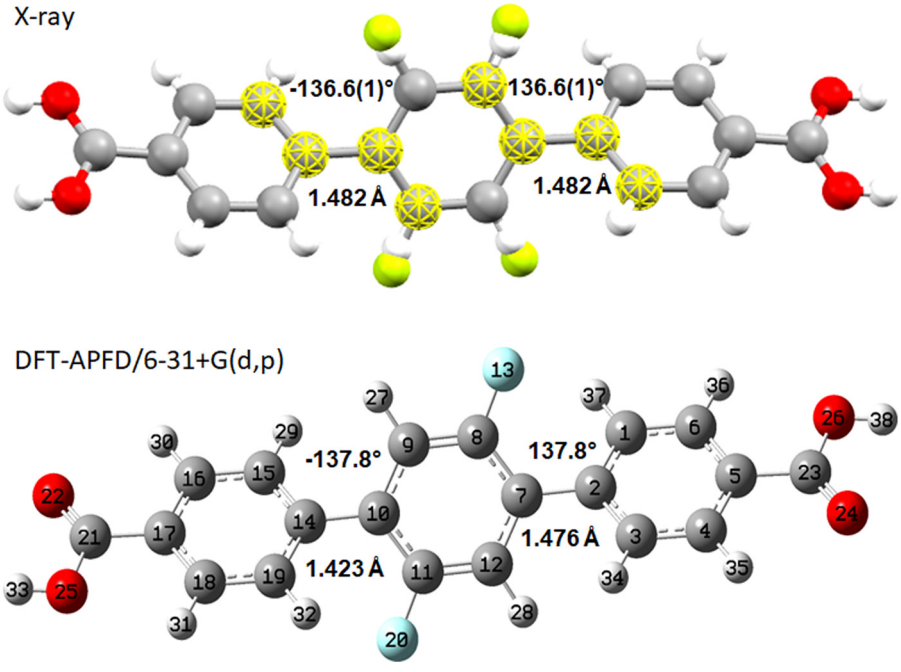

Fig. 6. Comparison between the structure determined by single crystal X-ray diffraction (top) and optimized geometry calculated with APFD/6–31+*G*(d,p) method (bottom) of compound **1**.

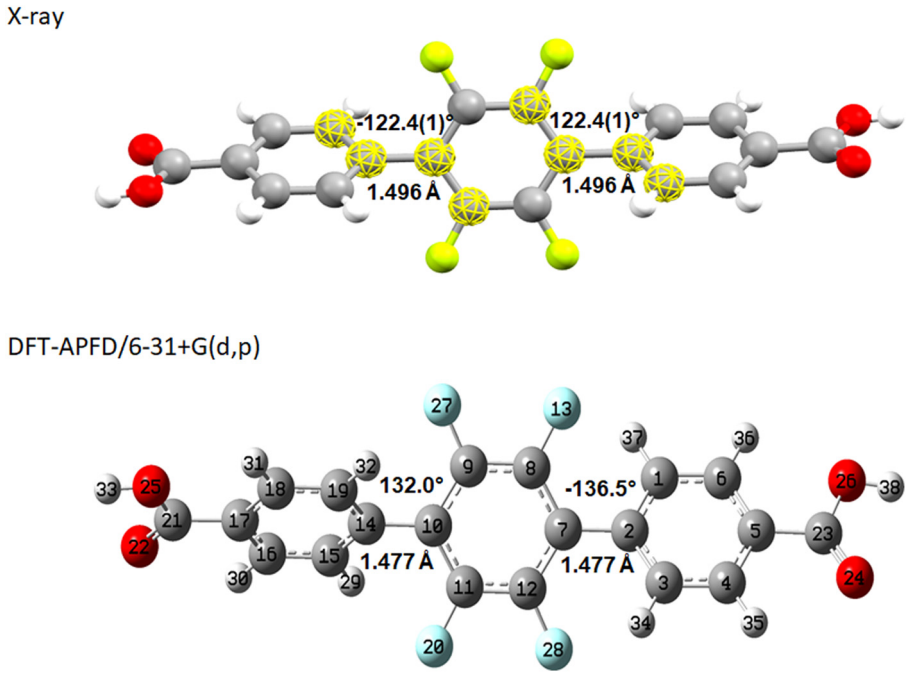

Fig. 7. Comparison between the structure determined by single crystal X-ray diffraction (top) and optimized geometry calculated with APFD/6–31+*G*(d,p) method (bottom) of compound **2**.

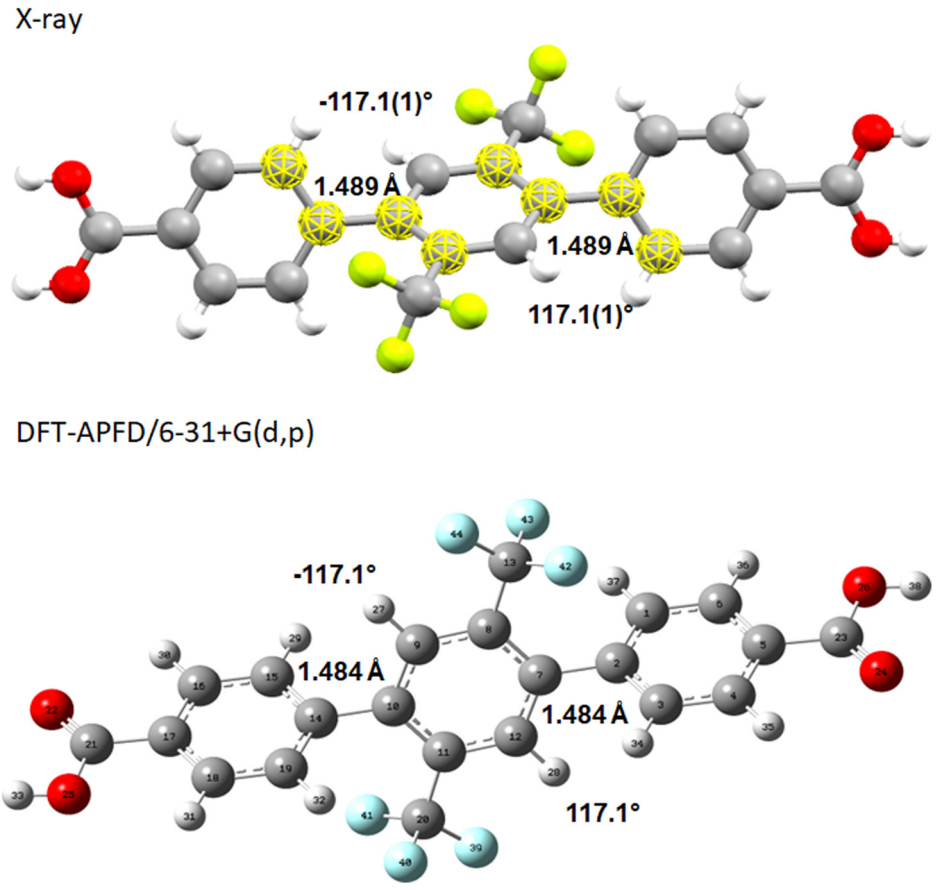

Fig. 8. Comparison between the structure determined by single crystal X-ray diffraction (top) and optimized geometry calculated with APFD/6–31+*G*(d,p) method (bottom) of compound 3.

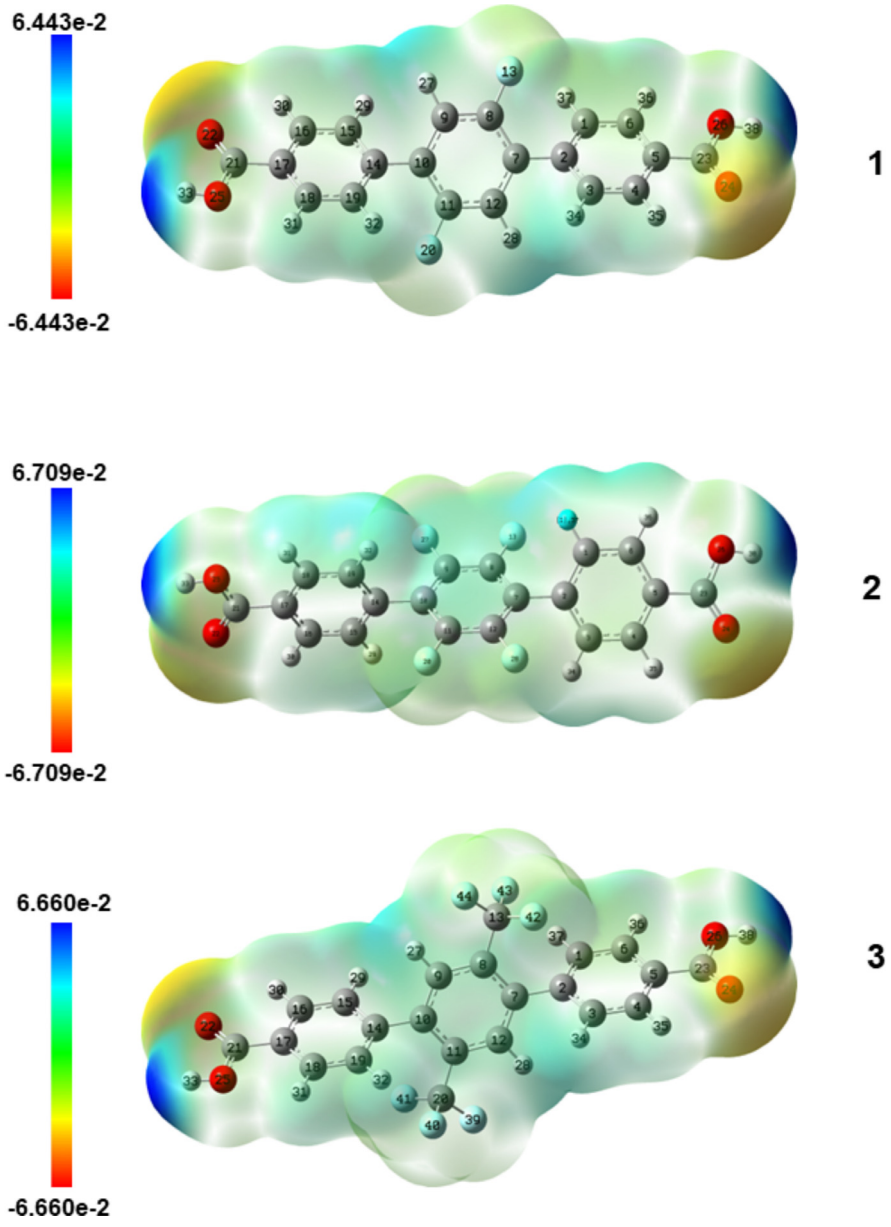

Fig. 9. Molecular electrostatic potential diagram of compounds **1, 2** and **3** performed at APFD/6–31+*G*(d,p) level of theory.

dral angles are around −137.8° and 137.8° in the case of compound **1**, 132.0° and −136.5° in case of **2**, and −117.1° and 117.1° for **3**, respectively. These values of dihedral angles indicate that the terminal phenyl rings are out of the plane defined by the central phenyl ring. The twisted orientation of both terminal phenyl rings is a result of the steric repulsion between fluorine atoms in the central phenyl ring and spatially neighboring hydrogen atoms in the terminal phenyl rings because the distances between these atoms in a theoretical fully planar structure of the terphenyl core are shorter than the sum of their van der Waals radii. The bond length (C7-C2) between the phenyl moieties was found to be over 1.450 Å, and therefore it has the character of a single carbon-carbon bond which can facilitate the distortional orientation in the terphenyl core. Because it is well known that highly electronegative fluorine can interact strongly with hydrogen atoms, a landscape of conformational investigation for each target compound was realized in order to identify any C-F···H-C intramolecular interaction that can be located on a local minimum of the potential energy surface, and glean the manner in which they affect the equilibrium molecular geometry. This conformational investigation includes a scan along one coordinate, namely C1-C2-C7-C8. This dihedral angle was the only one selected for the scan because all the molecular systems under investigation in this study are symmetrical. The scanning of the C1-C2-C7-C8 dihedral angle was performed in 20 steps (with an increment of 10°) starting from the coplanar orientation (180° or −180°) with geometry optimization at each point. The computational results are presented in Figs. S24–S26, and they indicate that the twisting effect is preferred, which means that no C-F···H–C intramolecular interaction occurs. Moreover, analysis of the landscape of conformational investigation led to the observation that the distortional conformation has been located into global minim of the potential energy. In order to gain some information on the nature of the interaction between F and H atoms, a plotting of noncovalent interaction (NCI) regions has been performed, as depicted in Figs. S27–S29. According to the NCI index, the attractive and repulsive interplay was identified as regions where $\rho \langle 0$ and $\rho \rangle 0$, respectively. These theoretical results showed that the weak interactions can be both van der Waals (labeled with green) and

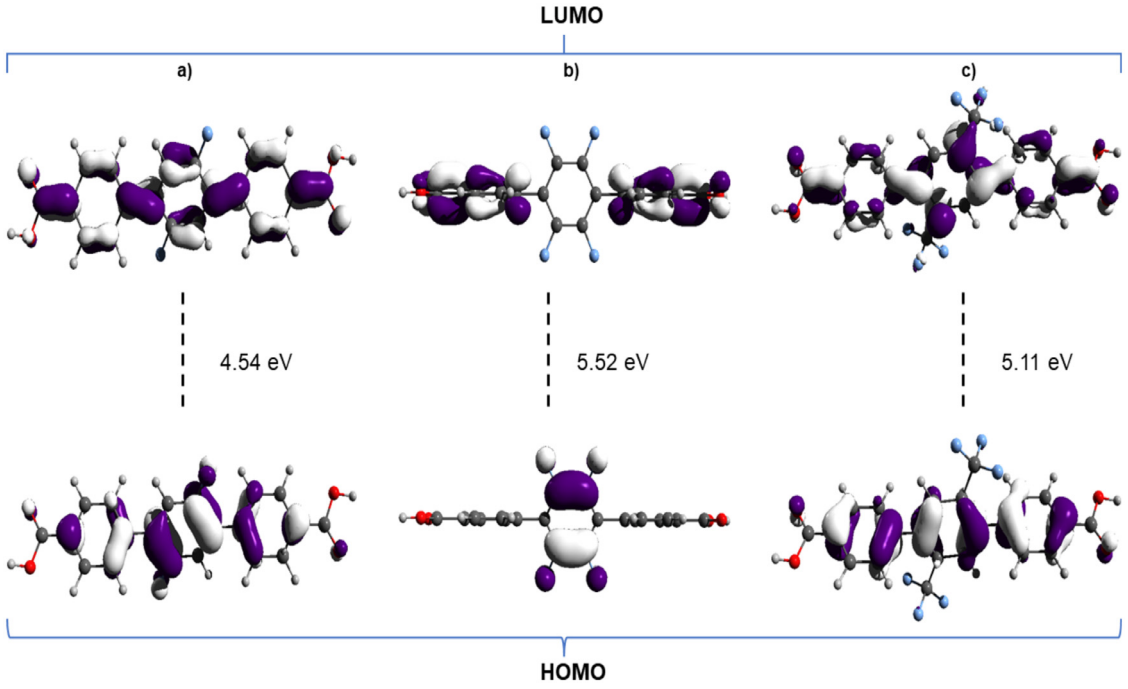

Fig. 10. Representation of frontier molecular orbitals and the estimation of energy band gap using the DFT-APFD/6–31+*G*(d,p) level of theory for the target compounds: (a) **1,** (**b**) **2 and** (**c**) **3**. The frontier molecular orbitals surface for HOMO and LUMO represented in mauve (dark) and white (intense) were drawn at 0.004 au isodensity level, respectively.

repulsive effects (labeled with red). However, the dominant interaction was the repulsive interplay in all three compounds, because the gradient density was $\rho > 0$ located to the 0.020 value. No attractive interactions (blue peaks) were observed, which could be a confirmation that a hydrogen bond can occur (Figs. S27–S29). The twisted orientation becomes favored, no weak C-F···H–C intramolecular interaction can occur, and the steric repulsion plays a much stronger role. This steric repulsion further substantiates the previous observation that distances between F groups and H atoms in a theoretical fully planar structure of the terphenyl core are shorter than the sum of their van der Waals radii.

This twisted orientation can determine a tridimensional spatial arrangement of a coordination complex during either synthesis or during a supramolecular arrangement. In the present work, the conformational effect predicted by the APFD/6–31+*G*(d,p) method was in agreement with the experimental X-ray data. However, a slight difference between the experimental data and calculation results has been observed for compound **2**, presumably due to the packing forces presented in the crystal that have not been accounted for in the theoretical investigation.

The chemical reactivity, chemical stability and active regions in chemical reactions of the target compounds were inferred from ESP representations and frontier HOMO-LUMO gap. The energy gap and ESP representations can offer a reliable result regarding the global reactivity descriptors in the identification of active sites in chemical structure or in the synthesis of new compounds [27,42,43]. Analysis of the ESP surface involves the identification of the regions of positive charge (the sites of nucleophilic attack) depicted in blue, neutral charge given in green, and negative region of the electrostatic potential (providing information about the sites where electrophilic attack can take place) shown in red. Taking into account the partial atomic charge diagrams in Fig. 9, the most positively charged site was found on the hydrogen atoms of the carboxyl groups, while the regions with negative charge were confirmed to be on the oxygen atoms of the carboxyl groups. In addition, estimation of positive and negative charge regions within the carboxyl functions confirms their ability to form hydrogen bond interactions with other functional groups, giving rise to dimer or trimer associations. Moreover, closer inspection of ESP diagrams revealed that the fluorine atoms do not represent the most negative regions, but rather present a slightly negative charge compared to the oxygen atoms from both carboxyl groups, which suggests an electronic reorganization in the whole molecular system. The ESP charge distribution estimated by DFT-APFD/6–31+*G*(d,p) calculations in the present work was in agreement with the Hirshfeld surfaces diagram (Figs. 3–5 and S21–S23).

The energy gap calculated with the DFT-APFD/6–31+*G*(d,p) method indicates that the reactivity trend is **1** > **3** > **2**, suggesting that the molecular system with the low number of fluorine atoms is more reactive (Fig. 10). This case is supported by the estimation of chemical hardness determined by $\eta = (-\text{EHOMO} + \text{ELUMO})/2$. According to the values of chemical hardness, a low energy gap indicates a soft molecule because electrons are promoted onto the higher energy state, which is associated with a more reactive molecule. The calculated chemical hardness value for compounds **1, 2** and **3** is approximately 2.27, 2.76, and 2.56 eV, and these values confirm that the molecular system **1** is more reactive than **3** or **2**. Also, the electron surface distribution in Fig. 10 indicates a change of density from HOMO to LUMO in all target compounds. This change of electron density appears as a delocalization from the central phenyl to the terminal phenyl rings. A clear delocalization can be observed in the case of compound **2**, when the strong cumulative effect of the four fluorine atoms directly attached to the central phenyl ring that push the electrons is assisted by the carboxyl groups that pull the electrons, leading to an electron release–withdrawing inductive effect.

4. Conclusions

A direct synthesis approach for the preparation of three linear therphenyl dicarboxylic acids bearing fluorine addends has been identified. The reaction yields of the Suzuki–Miyaura cross-

coupling reaction used to synthetize the compounds are superior to similar two-step attempts reported in the literature. The structure of each compound was confirmed by IR and NMR spectroscopy. The isolation of the three ligands in crystalline form allowed the structural confirmation by single crystal X-ray diffraction. The Hirschfield surface analysis was performed for each compound.

The computational results based on the DFT-APFD/6–31+*G*(d,p) level of theory reveal that the presence of the substituents (either fluorine atoms or trifluoromethyl groups) in the central phenyl ring in ortho positions relative to the terminal phenyl rings induces a twisting effect in all target compounds. The twisting effect can be due of the sterically repulsion between fluorine atoms in the central phenyl ring and spatially neighboring hydrogen atoms in the terminal phenyl rings because the distances between these atoms in a theoretical fully planar structure of the terphenyl core are shorter than the sum of van der Waals radii. Based on the quantum chemical calculations the chemical reactivity, chemical stability, and active regions in chemical reactions of the target compounds were estimated from ESP representations and frontier HOMO-LUMO gap. Moreover, the theoretical results predicted by ESP representation show the presence of the partially neutral charges on the fluorine atoms which explained the twisting effect.

Declaration of Competing Interest

The authors declare that they have no known competing financial interests or personal relationships that could have appeared to influence the work reported in this paper.

CRediT authorship contribution statement

Ioan-Andrei Dascalu: Conceptualization, Investigation, Writing – original draft, Writing – review & editing. **Dragos-Lucian Isac:** Investigation, Writing – original draft. **Sergiu Shova:** Investigation, Writing – original draft. **Mihaela Balan-Porcarasu:** Investigation, Writing – original draft. **Narcisa-Laura Marangoci:** Resources, Data curation. **Mariana Pinteala:** Resources, Data curation, Validation. **Christoph Janiak:** Investigation, Writing – original draft, Supervision.

Acknowledgements

This work was supported by a grant of the Romanian Ministry of Education and Research, CNCS - UEFISCDI, project number PN-III-P1-1.1-PD-2019-1303, within PNCDI III.

The financial support of European Social Fund for Regional Development, Competitiveness Operational Programme Axis 1 - POCPOLIG (ID P_37_707, Contract 67/08.09.2016, cod MySMIS: 104810) is gratefully acknowledged.

Supplementary materials

Supplementary material associated with this article can be found, in the online version, at doi:10.1016/j.molstruc.2022.133474.

References

[1] Ü. Kökçam-Demir, A. Goldman, L. Esrafili, M. Gharib, A. Morsali, O. Weingart, C. Janiak, Coordinatively unsaturated metal sites (open metal sites) in metal–organic frameworks: design and applications, Chem. Soc. Rev. 49 (2020) 2751–2798.
[2] J. Zhou, G. Tian, L. Zeng, X. Song, Xw. Bian, Nanoscaled metal-organic frameworks for biosensing, imaging, and cancer therapy, Adv. Healthc. Mater. 7 (2018) 1800022.
[3] D.M. Steinert, S.J. Ernst, S.K. Henninger, C. Janiak, Metal-organic frameworks as sorption materials for heat transformation processes, Eur. J. Inorg. Chem. 28 (2020) 4502–4515.
[4] O.M. Yaghi, Reticular chemistry: molecular precision in infinite 2D and 3D, Mol. Front. J. 3 (1) (2019) 66–83.
[5] O.M. Yaghi, M. O'Keeffe, N.W. Ockwig, H.K. Chae, M. Eddaoudi, J. Kim, Reticular synthesis and the design of new materials, Nature 423 (2003) 705–714.
[6] F.A. Almeida Paz, J. Klinowski, S.M.F. Vilela, J.P.C. Tomé, J.A.S. Cavaleiroc, J. Rochaa, Ligand design for functional metal-organic frameworks, Chem. Soc. Rev. 41 (2012) 1088–1110.
[7] K.K. Tanabea, S.M. Cohen, Postsynthetic modification of metal–organic frameworks-a progress report, Chem. Soc. Rev. 40 (2011) 498–519.
[8] M. Kalaj, S.M. Cohen, Postsynthetic modification: an enabling technology for the advancement of metal–organic frameworks, ACS Cent. Sci. 6 (7) (2020) 1046–1057.
[9] Z. Wang, S.M. Cohen, Postsynthetic modification of metal–organic frameworks, Chem. Soc. Rev. 38 (2009) 1315–1329.
[10] T.H. Chen, I. Popov, O. Zenasni, O. Daugulis, O.Š. Miljanić, Superhydrophobic perfluorinated metal–organic frameworks, Chem. Commun. 49 (2013) 6846–6848.
[11] C.Xia Chen, Z.W. Wei, Q.F. Qiu, Y.Z. Fan, C.C. Cao, H.P. Wang, J.J. Jiang, D. Fenske, C.Y. Su, A porous Zn(II)-metal-organic framework constructed from fluorinated ligands for gas adsorption, Cryst. Growth Des. 17 (4) (2017) 1476–1479.
[12] Z. Zhang, O.Š. Miljanić, Fluorinated organic porous materials, Org. Mater. 1 (2019) 19–29.
[13] Si. Noro, T. Nakamura, Fluorine-functionalized metal–organic frameworks and porous coordination polymers, NPG Asia Mater. 9 (2017) e433.
[14] P. Pachfule, R. Das, P. Poddar, R. Banerjee, Structural, magnetic, and gas adsorption study of a series of partially fluorinated metal-organic frameworks (HF-MOFs), Inorg. Chem. 50 (2011) 3855–3865.
[15] D.S. Zhang, Z. Chang, Y.F. Li, Z.Y. Jiang, Z.H. Xuan, Y.H. Zhang, J.R. Li, Q. Chen, T.L. Hu, X.H. Bu, Fluorous metal-organic frameworks with enhanced stability and high H_2/CO_2 storage capacities, Sci. Rep. 3 (2013) 3312.
[16] C. Yang, U. Kaipa, Q.Z. Mather, X. Wang, V. Nesterov, A.F. Venero, M.A. Omary, J. Am. Chem. Soc. 133 (45) (2011) 18094–18097.
[17] D. Balestri, I. Bassanetti, S. Canossa, C. Gazzurelli, A. Bacchi, S. Bracco, A. Comotti, P. Pelagatti, Cryst. Growth Des. 18 (11) (2018) 6824–6832.
[18] D.D. Zhang, Z. Chang, Y.F. Li, Z.Y. Jiang, Z.H. Xuan, Y.H. Zhang, J.R. Li, Q. Chen, T.L. Hu, X.H. Bu, Fluorous metal-organic frameworks with enhanced stability and high H2/CO2 storage capacities, Sci. Rep. 3 (2013) 3312.
[19] Y. Kima, T.M. Swager, Ultra-photostable n-type PPVs, Chem. Commun. 3 (2005) 372–374.
[20] Rigaku Oxford Diffraction, CrysAlisPro Software system, Version 1.171.41.64, Rigaku Corporation, Oxford, UK, 2015.
[21] O.V. Dolomanov, L.J. Bourhis, R.J. Gildea, J.A.K. Howard, H. Puschmann, OLEX2: a complete structure solution, refinement and analysis program, J. Appl. Crystallogr. 42 (2009) 339–341.
[22] G. Sheldrick, SHELXT - Integrated space-group and crystal-structure determination, Acta Crystallogr. A 71 (2015) 3–8.
[23] G. Sheldrick, Crystal structure refinement with SHELXL, Acta Crystallogr. Sect. C 71 (2015) 3–8.
[24] M. Frisch, G. Trucks, H. Schlegel, et al., Gaussian 16 G. Scuseria, M. Robb, J. Cheeseman, G. Scalmani, V. Barone, G. Petersson, H. Nakatsuji, X. Bao, M. Caricato, A. Marenich, J. Bloino, B. Janesko, R. Gomperts, B. Mennucci, H. Hratchian, J. Ortiz, A. Izmaylov, J. Sonnenberg, D. Williams-Young, F. Ding, F. Lipparini, F. Egidi, J. Goings, B. Peng, A. Petrone, T. Henderson, D. Ranasinghe, V. Zakrzewski, J. Gao, N. Rega, G. Zheng, W. Liang, M. Hada, M. Ehara, K. Toyota, R. Fukuda, J. Hasegawa, M. Ishida, T. Nakajima, Y. Honda, O. Kitao, H. Nakai, T. Vreven, K. Throssell, J. Montgomery Jr, J. Peralta, F. Ogliaro, M. Bearpark, J. Heyd, E. Brothers, K. Kudin, V. Staroverov, T. Keith, R. Kobayashi, J. Normand, K. Raghavachari, A. Rendell, J. Burant, S. Iyengar, J. Tomasi, M. Cossi, J. Millam, M. Klene, C. Adamo, R. Cammi, J. Ochterski, R. Martin, K. Morokuma, O. Farkas, J. Foresman and D. Fox, Gaussian Inc., Wallingford CT, 2016.
[25] A. Austin, G.A. Petersson, M. Frisch, F.J. Dobek, G. Scalmani, K. Throssell, A density functional with spherical atom dispersion terms, J. Chem. Theory Comput. 8 (2012) 4989–5007.
[26] R. Ditchfield, W.J. Hehre, J.A. Pople, Self-consistent molecular-orbital methods. IX. An extended Gaussian-Type basis for molecular-orbital studies of organic molecules, J. Chem. Phys. 54 (1971) 724–728.
[27] B.I. Bratanovici, C. Cojocaru, A. Nicolescu, M. Dascalu, G. Roman, Di-topic hybrid ligands with an isoxazole ring in the central unit: synthesis, structural characterization and molecular modeling, J. Mol. Struct. 1245 (2021) 131129.
[28] D.C. Alamo, T.R. Cundari, DFT and TDDFT study of the reaction pathway for double intramolecular C–H activation and functionalization by iron, cobalt, and nickel–nitridyl complexes, Inorg. Chem. 60 (16) (2021) 12299–12308.
[29] R. Dennington, T.A. Keith, J.M. Millam, GaussView, Version 6.1, Semichem Inc., Shawnee Mission, KS, USA, 2016 official website https://gaussian.com/gaussview6/ .
[30] M.D. Hanwell, D.E. Curtis, D.C. Lonie, T. Vandermeersch, E. Zurek, G.R. Hutchison;, Avogadro: an advanced semantic chemical editor, visualization, and analysis platform, J. Cheminform. 4 (2012) 17.
[31] T. Lu, F. Chen, Multiwfn: a multifunctional wavefunction analyzer, J. Comput. Chem. 33 (2012) 580–592.
[32] J. Contreras-García, E.R. Johnson, S. Keinan, R. Chaudret, J.P. Piquemal, D.N. Beratan, W. Yang, NCIPLOT: a program for plotting noncovalent interaction regions, J. Chem. Theory Comput. 7 (2011) 625–632.
[33] E.R. Johnson, S. Keinan, P. Mori-Sanchez, J. Contreras-Garcıa, A.J. Cohen, W. Yang, Revealing noncovalent interactions, J. Am. Chem. Soc. 132 (2010) 6498–6506.

[34] W. Humphrey, A. Dalke, K. Schulten, VMD – Visual Molecular Dynamics, J. Mol. Graph. 14 (1996) 33–38.
[35] Gnuplot 5.4 An Interactive Plotting Program, http://www.gnuplot.info/ (accessed April 2022).
[36] N. Miyaura, A. Suzuki, Palladium-catalyzed cross-coupling reactions of organoboron compounds, Chem. Rev. 95 (7) (1995) 2457–2483.
[37] David Blakemore, Chapter 1: Suzuki–Miyaura Coupling, in: Synthetic Methods in Drug Discovery, Volume 1, Royal Society of Chemistry, 2015, pp. 1–69, doi:10.1039/9781782622086-00001. Volume 1.
[38] H. Wang, L. Yu, Y. Lin, J. Peng, S.J. Teat, L.J. Williams, J. Li, Adsorption of fluorocarbons and chlorocarbons by highly porous and robust fluorinated zirconium metal−organic frameworks, Inorg. Chem. 59 (2020) 4167–4171.
[39] J. Peter, in: Infrared and Raman spectroscopy: principles and spectral interpretation, first ed., Elsevier, 2011, p. 109.
[40] M.J. Turner, J.J. McKinnon, S.K. Wolff, D.J. Grimwood, P.R. Spackman, D. Jayatilaka, M.A. Spackman, CrystalExplorer21.5, Version 21.5, University of Western Australia, 2021 © 2005-2021 https://crystalexplorer.net/.
[41] (a) J.J. McKinnon, M.A. Spackman, A.S. Mitchell, Novel tools for visualizing and exploring intermol-ecular interactions in molecular crystals, Acta Cryst. B60 (2004) 627–668; (b) M.A. Spackman, J.J. McKinnon, Fingerprinting intermolecular interactions in molecular crystals, CrystEngComm 4 (2002) 378–392; (c) J.J. McKinnon, D. Jayatilaka, M.A. Spackman, Towards quantitative analysis of intermolecular interactions with Hirshfeld surfaces, Chem. Commun. (2007) 3814–3816; (d) P.R. Spackman, M.J. Turner, J.J. McKinnon, S.K. Wolff, D.J. Grimwood, D. Jayatilaka, M.A. Spackman, CrystalExplorer: a program for Hirshfeld surface analysis, visualization and quantitative analysis of molecular crystals, J. Appl. Cryst. 54 (2021) 1006–1011.
[42] A. Airinei, D.L. Isac, M. Homocianu, C. Cojocaru, C. Hulubei, Solvatochromic analysis and DFT computational study of an azomaleimide derivative, J. Mol. Liq. 240 (2017) 476–485.
[43] Y. Oueslati, S. Kansız, A. Valkonen, T. Sahbani, N. Dege, W. Smirani, Synthesis, crystal structure, DFT calculations, Hirshfeld surface, vibrational and optical properties of a novel hybrid non-centrosymmetric material (C10H15N2)2H2P2O7, J. Mol. Struct. 1196 (2019) 499–507.